

## Article

# Performance of Atmospheric Plasma-Sprayed Thermal Barrier Coatings on Additively Manufactured Super Alloy Substrates

Madhura Bellippady <sup>1,\*</sup>, Stefan Björklund <sup>1</sup>, Xin-Hai Li <sup>2</sup>, Robert Frykholm <sup>3</sup>, Bjorn Kjellman <sup>4</sup>, Shrikant Joshi <sup>1</sup>  
and Nicolaie Markocsan <sup>1</sup>

<sup>1</sup> Department of Engineering Science, University West, 461 32 Trollhättan, Sweden

<sup>2</sup> Siemens Energy AB, 612 31 Finspang, Sweden

<sup>3</sup> Hoganas AB, 263 39 Hoganas, Sweden

<sup>4</sup> GKN Aerospace AB, 461 38 Trollhättan, Sweden

\* Correspondence: madhura.bellippady@hv.se

**Abstract:** This work represents a preliminary study of atmospheric plasma-sprayed (APS) Ytria-Stabilized Zirconia (YSZ)-based thermal barrier coatings (TBCs) deposited on forged and additive manufactured (AM) HAYNES<sup>®</sup>282<sup>®</sup> (H282) superalloy substrates. The effect of different feedstock morphologies and spray gun designs with radial and axial injection on APS-deposited YSZ layer characteristics such as microstructure, porosity content, roughness, etc., has been investigated. The performance of TBCs in terms of thermal cycling fatigue (TCF) lifetime and erosion behaviour were also comprehensively investigated. In view of the high surface roughness of as-built AM surfaces compared to forged substrates, two different types of NiCoCrAlY bond coats were examined: one involved high-velocity air fuel (HVOF) spraying of a finer powder, and the other involved APS deposition of a coarser feedstock. Despite the process and feedstock differences, the above two routes yielded comparable bond coat surface roughness on both types of substrates. Variation in porosity level in the APS topcoat was observed when deposited using different YSZ feedstock powders employing axial or radial injection. However, the resultant TBCs on AM-derived substrates were observed to possess similar microstructures and functional properties as TBCs deposited on reference (forged) substrates for any given YSZ deposition process and feedstock.

**Keywords:** additive manufacturing; thermal barrier coatings; superalloys; microstructural characterization; thermal cycling; erosion testing



**Citation:** Bellippady, M.; Björklund, S.; Li, X.-H.; Frykholm, R.; Kjellman, B.; Joshi, S.; Markocsan, N. Performance of Atmospheric Plasma-Sprayed Thermal Barrier Coatings on Additively Manufactured Super Alloy Substrates. *Coatings* **2024**, *14*, 626. <https://doi.org/10.3390/coatings14050626>

Academic Editor: Narottam P. Bansal

Received: 2 March 2024

Revised: 3 May 2024

Accepted: 10 May 2024

Published: 15 May 2024



**Copyright:** © 2024 by the authors. Licensee MDPI, Basel, Switzerland. This article is an open access article distributed under the terms and conditions of the Creative Commons Attribution (CC BY) license (<https://creativecommons.org/licenses/by/4.0/>).

## 1. Introduction

Despite being regarded as the cleanest of the standard fossil-fuel power generating technologies, gas turbines powered by hydrocarbon-based fuels emit significant CO<sub>2</sub> emissions (about 440 gCO<sub>2</sub>/kWh for natural gas). Vast efforts have been made in past decades to improve gas turbine efficiency and consequently reduce CO<sub>2</sub> emissions. Most improvements were mainly attained by 1. integrating structural materials with high thermal stability, 2. incorporating advanced thermal barrier coatings (TBCs), 3. improving cooling efficiency, etc. [1–3]. Ni-based superalloys with appealing high-temperature strength have been widely employed in the engine's hot section components (combustor and turbine blades) with temperatures surpassing 1000 °C. Further improvements in TBCs and the incorporation of complex-shaped cooling channels for enhanced effectiveness have enabled the industry to raise gas input temperatures to 1500 °C, thus increasing thermal efficiency and the thrust-to-weight ratio and lowering noxious by-product emissions [3,4]. In the above context, it is acknowledged that traditional substrate production procedures, e.g., those involving subtractive manufacturing, are limited with regard to generating complex shaped Ni-based structural materials and with incorporating efficient cooling systems. Additive manufacturing (AM) is a digital manufacturing technology that has seen

promising progress in recent decades to produce components from 3D model data, usually layer upon layer, as opposed to subtractive manufacturing methods. This unique approach makes AM the potential future production process for building intricate geometries such as gas turbine components while significantly reducing material utilization and costs [5,6].

HAYNES 282 (H282) alloy has a distinct combination of creep strength (649 to 927 °C), thermal stability, and fabricability exceeding that of commercial Waspaloy and approaching that of R-41 alloy [7]. Regardless of the different processes used in additive manufacturing techniques, AM generally employs a laser beam or an electron beam as a heat source to melt metallic powder, wire, or sheet. Electron Beam Powder Bed Fusion (EB-PBF) is one of the most widely employed AM techniques for building Ni-based super alloy complex geometry parts with promising material characteristics, such as low residual stress and low material contamination [8,9]. The AM approach is especially desirable for manufacturing complex gas turbine components that were previously made in several parts and then welded together. This method allows the production of these components at once, including internal cooling channels, thus saving substantial quantities of expensive superalloy materials. Regardless of the proven advantages of AM processing, its viability to replace traditional manufacturing techniques is still being researched extensively; for example, the capacity to make defect-free, consistent quality components with the specified surface texture. The built-in flaws characteristic of EB-PBF processes, such as surface defects/irregularities (surface roughness, open pores, surface cracks, pits, etc.) and bulk defects (round pores, shrinkage pores, lack of fusion defects), are inevitable in AM-built components [10]. This demands the use of various post-treatments and surface engineering techniques to be employed on the AM built components before they can be used in actual application. Thermal post-treatments, such as Hot Isostatic Press (HIP), have been frequently used on EB-PBF components to seal internal pores/defects and enhance material properties [11]. However, the surface features remain unaltered and rough after being treated with a HIP.

As has been widely documented, TBCs play a vital role in enhancing the high-temperature capability of superalloy components, and AM-built parts are no exception. Thus, even if the components are produced by AM technologies, protective TBCs will be needed to enable structural AM components to encounter a wider range of environments and operational temperatures in actual service. Since the surface properties of as-built AM components can have a significant impact on TBC performance and longevity, it necessitates a detailed evaluation of properties and performance of TBCs developed on as AM-built surfaces deploying various powder feedstocks and spray gun systems and compared with TBCs identically deposited on conventional forged substrates. Mobin et al. [11] studied the performance of HVAF-sprayed NiCoCrAlY coating on EB-PBF-built Alloy 718 substrates. In this research, authors used the HIP treatment on the as-built and coated specimens to seal the interior pores and thus enhance the oxidation resistance. However, they found that treatment via HIP improved the oxidation resistance of uncoated Alloy 718 while negatively affecting the oxidation behaviour of coated Alloy 718.

However, it is of utmost importance to have suitable TBCs developed employing appropriate deposition processes to impart improved surface characteristics and enhance the temperature capability of AM superalloy substrates. The longevity of a TBC system depends on the bond coat microstructure and the topcoat–bond coat interface topography [12,13], both of which are intimately linked to the deposition methods used. In general, for APS TBCs, NiCoCrAlY bond coats deposited by APS, high-velocity oxy-fuel (HVOF) spraying, or Vacuum Plasma Spraying (VPS) are widely employed. In our previous work [14], HVAF has shown promising results as a bond coat deposition method with a potential reduction in AM substrate surface asperities and yielding adequate bonding to the SPS topcoat. HVAF is an energy efficient bond coat deposition method as it employs compressed air as an oxidant instead of oxygen as in the case of HVOF, and unlike in VPS, components are coated in an ambient atmosphere. HVAF is also a more suitable process than APS and HVOF due to the higher particle velocity and lower in-flight particle temperature, which, in turn, results in dense coating with minimal oxide formation [12].

Recent studies from this group on suspension plasma sprayed TBCs on AM substrates demonstrated that high-velocity air fuel (HVOF) sprayed NiCoCrAlY bond coats can reduce the asperities present on AM substrates, and the subsequent Suspension Plasma Spray (SPS) deposited YSZ layers exhibit similar microstructures and properties as those deposited on conventional substrates [14]. Another attempt wherein low thermal conductivity coatings were studied by Markocsan et al. [15] investigated YSZ coatings sprayed using two feedstock morphologies (agglomerated and sintered and plasma-spheroidized HOSP) using APS. They demonstrated that coating thermal properties are significantly influenced by the powder morphology, porosity level and spray parameters. Combinations of different Suspension Plasma Spray coatings together with HVOF, APS and HVOF bond coats tested against conventional segmented APS coatings were investigated by Nicholas et al. [16]. They noted variations in microstructure among SPS coatings applied on HVOF, HVOF, and APS bond coats, attributed to differences in the surface roughness of the bond coats. In all the cases, the primary focus has been on lifetime testing of these new coating systems with varying feedstock morphology, spray parameters, bond coat deposition techniques, etc. Thus, one of the objectives of this study is also to investigate, apart from the effect of different substrates (AM and forged), attempts to deposit bond coats by different techniques such as HVOF and commercial APS.

The present study investigates the coating microstructure and thermal stability of APS-deposited YSZ on reference, and AM substrates with APS/HVOF deposited NiCrCoAlY bond coats. Further, the YSZ coating performance on AM-built and reference substrates have been compared for different feedstock powder morphologies, bond coat deposition methods, and plasma spray gun systems with radial and axial feed capability. There are several studies on the influence of powder feedstock, bond coat and spray gun systems on YSZ coating performance on forged (reference) substrates [17–19]. However, to the best of the authors' knowledge such an investigation on APS coatings on AM-built substrates along a comparison with reference substrates has never been attempted. Moreover, TBCs on AM components are an area of enormous technological relevance to future gas turbine engines.

## 2. Experimental Details

### 2.1. Preparation of the Additive Manufactured Substrates

The AM substrate specimens built from the H282 superalloy were produced by the EB-PBF process. Gas atomized powder feedstock AMPERPRINT®0233.002 with a nominal particle size range of 45–90 µm supplied by Höganäs AB (Höganäs AB, Hoganas, Sweden) was utilized for the EB-PBF process. The chemical composition of the powder utilized is given in Table 1. AM-built square plates of dimensions 60 mm × 60 mm × 6 mm were manufactured using an Arcam A2X system (Arcam AB, Mölnlycke, Sweden), and disc coupons (25.4 mm dia.) were cut out from them by water jet cutting for subsequent coating deposition studies. To facilitate direct comparison, along with AM-built substrates, forged H282 (reference) coupons of identical size were also acquired (Haynes International, Kokomo, IN, USA). Figure 1 shows an EB-PBF-built H282 plate and a disc coupon after water jet cutting.

**Table 1.** Typical chemical composition of the AMPERPRINT®0233.002 H282 powder [19].

Element	Cr	Co	Mo	Ti	Al	C	B	Ni
Wt.%	19.5	10	8.5	2.1	1.5	0.05	0.005	Balance

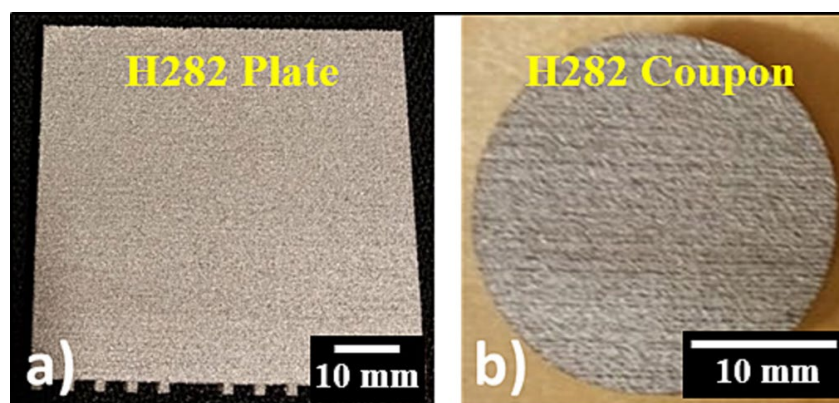


**Figure 1.** Photographs of (a) a plate produced by the EB-PBF process and (b) a disc coupon cut from the plate via water jet cutting.

### 2.2. Deposition of HVOF and APS Bond Coats

Bond coat deposition on AM substrates was carried out with an HVOF M3™ supersonic spray torch-axial injection (Uniqucoat Technologies, Oilville, VA, USA) using a gas atomized NiCoCrAlY feedstock powder (AMPERIT405.001-Höganäs AB, Hoganas, Sweden) with particle size range 22–45  $\mu\text{m}$ . A second set of bond coats on AM and forged substrates were applied using APS-F4-MB gun (radial injection), also using a gas atomized NiCoCrAlY feedstock powder (AMPERIT405.002-Höganäs AB, Hoganas, Sweden) but with a coarser particle size range of 45–90  $\mu\text{m}$ . The forged substrates were subjected to alumina grit blasting prior to spraying, whereas the AM substrates were sprayed in as-built condition as they appeared to exhibit adequate surface roughness in this form. The chemical composition of the NiCoCrAlY powder feedstock is shown in Table 2. The standard parameters (HVOF and APS) are given by the equipment manufacturer and were used to deposit the bond coatings [20].

**Table 2.** Typical chemical composition of the AMPERIT 405.001 and AMPERIT 405.002 NiCoCrAlY powder [21].

Element	Co	Cr	Al	Y	Hf	Si	All Others, Each	Ni
Wt.%	21.0–23.0	16.0–18.0	11.8–13.2	0.4–0.8	0.1–0.3	0.2–0.6	Max. 0.1	Balance

### 2.3. Topcoat Deposition

The APS method was used to deposit the topcoat with four different spray conditions (two parameter sets employ two distinct plasma spray guns) using two following types of 8 wt.% Yttria-Stabilized Zirconia (8YSZ) feedstock powders of particle size 45–125  $\mu\text{m}$ : (i) agglomerated and sintered (A&S), designated as Powder 1—AMPERIT827.006 (Hoganas AB, Sweden); and (ii) plasma spheroidized/HOSP powder, designated as Powder 2—AMPERIT831.006 (Hoganas AB, Sweden). The feedstock powder morphology is crucial in plasma spraying since the shape and size distribution of individual powder particles, apart from the processing conditions, has a major influence on the quality of the coating produced. The SEM morphologies of A&S and HOSP feedstock powders are shown in Figure 2. The HOSP powders have been reported to offer high thermal spray deposition efficiency [22]. The two spray guns employed were F4-MB (Oerlekon Metco, Wohlen, Switzerland) with radial injection and AXIAL III with axial injection (Northwest Mettech Corp., Surrey, BC, Canada). With these combinations, four spray conditions, Run 1 to Run 4, were utilized to deposit topcoats on three different substrates and bond coat compositions. The spray parameters for Runs 3 and 4 are as specified in Table 3, and for Runs 1 and 2 are discussed elsewhere [15].

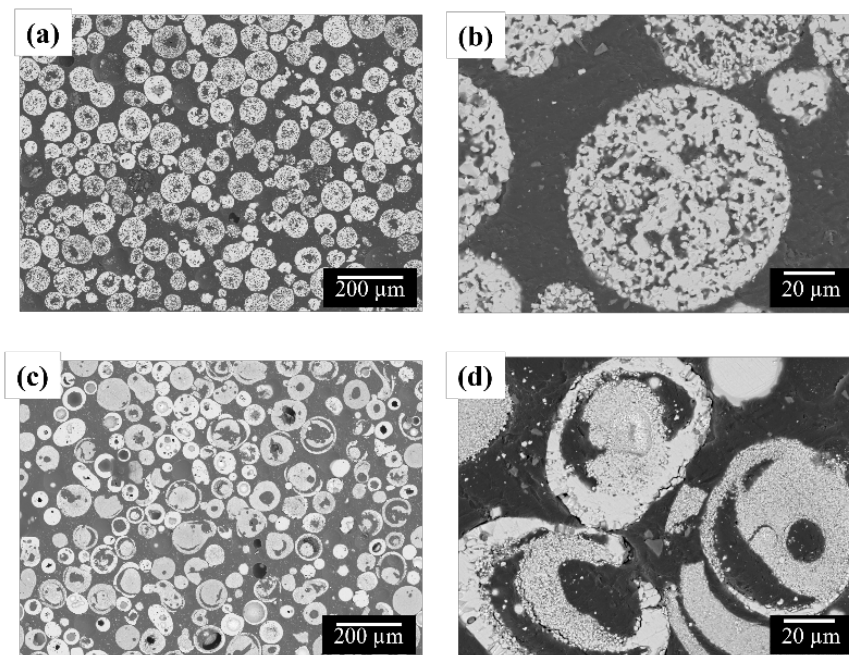


**Figure 2.** SEM morphology of the feedstock powders. (a) YSZ AMPERIT827.006-agglomerated and sintered and (c) YSZ AMPERIT831.006-plasma spheroidized hollow spherical, (b,d) magnified images respectively.

**Table 3.** Spray parameters for APS 8YSZ topcoat deposition for Run 3 and Run 4.

Spray Run	Feedstock Powder	Spray Gun	Nozzle	Total Gas Flow (L/min)	Current (A)	Stand of Distance (mm)	Surface Speed (m/min)	Powder Feed (g/min)	Strokes
Run 3	AMPERIT831.006	Axial III	12ST	150	230	150	100	96	13
Run 4	AMPERIT827.006	Axial III	12ST	150	230	150	100	151	8

Hereafter, forged H282 coated samples with APS bond coat from Run 1 to 4 are considered reference samples. Table 4 summarizes the spray parameters employed for all four spray runs of topcoat deposition, two sets each with a radial and axial injection of feedstock. Thus, in total, there were 12 sets of coatings prepared with 4 different topcoat parameters and 3 distinct substrate–bond coat combinations as described above.

**Table 4.** Number of samples tested and sample labelling for different combinations of substrate and bond coat deposition methods.

Sl. No.	Spray Run	Substrate and Bond Coat Deposition Method	Sample Labelling
1	Run 1 AMP827.006 F4-MB radial gun		
2	Run 2 AMP831.006 F4-MB radial gun	Additive Manufactured substrate + High-Velocity Air Fuel sprayed bond coat (AM/HVAF)	AM/HVAF
3	Run 3 AMP831.006 Axial gun	Additive Manufactured substrate + Atmospheric Plasma Sprayed bond coat (AM/APS)	AM/APS
4	Run 4 AMP827.006 Axial gun	Forged H282 substrate + Atmospheric Plasma Sprayed bond coat (Ref./APS)	Reference/APS

#### 2.4. Heat-Treatment of the Sprayed Samples

Before subjecting to further functional characterization, the coatings were heat treated in a vacuum furnace to initiate age hardening of the H282 material.

A standard age hardening treatment for the H282 superalloy [23] was executed in two distinct steps:

Step 1: 1010 °C for 2 h with subsequent air-cooling.

Step 2: 788 °C for 8 h with subsequent air-cooling.

#### 2.5. Surface Roughness Measurements

An attempt was made to measure the roughness to assess the arithmetic average roughness (Ra) of the bare substrate (reference and AM built) and bond coats developed by HVAF/APS processes. The arithmetic average roughness of the substrates and bond coats was determined on the 3D surface topography images of the samples obtained by white light interferometry (WLI). The use of WLI allows for deeper investigation into the asperities; thus, this approach delivers more precise roughness data. The 3D surface topography images of the substrates and bond coats were obtained using the 3D-profilometer Profilm3D (Filmetrics, Inc., San Diego, CA, USA). The 3D profilometer employs the WLI technique, which relies on the Michelson interferometry principle to produce topographic images of a coating surface. The following device specifications were used for WLI measurements: system 19K004, objective Nikon 10× DI, zoom 4×, and normal speed. The scan configuration, stitch parameters, and post-processing steps performed to acquire the 3D surface topography images are shown in Table 5. For each substrate bond coat data, 10 Ra measurements were recorded in accordance with ISO4287 [24] Amplitude, and the average was computed with the associated standard deviation.

**Table 5.** Scan configuration, stitch parameters, and post-processing steps (Profilm3D software 2018).

<b>Scan</b>	Back scan/Scan Length	400 µm/800 µm
	Analysis Type	Envelope Peak/1.8%
	Grid Total Area	1200 µm × 1000 µm/9 pictures
<b>Stitch</b>	Type/Method/Details	3 × 3/Overlap: 0.5%/Cropped to inter rectangle
<b>Post-Processing</b>	N°1–Fill in invalids	Method Interpolate invalids from neighbour pixels
	N°2–Spatial Filter	Type Smoothed /Method Median/5 × 5 pixels

#### 2.6. Microstructural Characterizations

The feedstock powder and coating cross-section morphology analysis of metallographically prepared samples were conducted using a Hitachi TM3000 (Tokyo, Japan) scanning electron microscope (SEM) equipped with an energy dispersive spectroscope. The SEM images were post-processed using image J 1.53k (ImageJ bundled with 64-bit Java 1.8.0\_112, National Institutes of Health, Bethesda, MD, USA) to determine the porosity distribution in the topcoat. SEM cross-sectional images were acquired at magnifications of 500× and 5000× to measure coarse and fine porosity, with 20 SEM images recorded for each magnification. For each TBC sample an average with standard deviation was calculated from the 20 measurements obtained. Finally, the sum of the coarse and fine porosity was used to compute the overall average porosity of the topcoat.

#### 2.7. Erosion Tests

The TBC on AM samples were subjected to room-temperature erosion tests using an air-jet erosion tester TR-470 (Ducom Instruments, Groningen, The Netherlands) in accordance with ASTM G76-07 [25]. An oven-dried (150 °C for 12 h) alumina powder of average particle size of 50 ± 5 µm was used as erosive media. Three erosion tests were attempted on each of the TBC on AM substrates at different locations. To estimate the erosion rate, the weight of the sample was measured before and after the erosion test

using a sensitive balance (PCE-AB 100 Instruments, Southampton, UK). Table 6 shows the parameters utilized for erosion testing.

**Table 6.** Parameters used for erosion testing.

Parameters	Values
Impingement angle	90°
Erodent feed rate	2 g/min
Pressure	0.25 bar
Time	4 min
Erodent velocity	30 m/s
Stand-off distance	10 mm
Nozzle diameter	1.5 mm
Impact angle	90°
Carrier media	Air
Temperature	Room temperature

### 2.8. Thermal Cyclic Fatigue Testing

Thermal cyclic fatigue (TCF) testing was performed to evaluate the lifespan of the YSZ topcoat with an HVOF bond coat on AM substrates and an APS bond coat on reference substrates. The TCF testing was carried out in an automated furnace (Entech ECF 14/16, Ängelholm, Sweden) under a normal atmospheric condition. TBC samples were heated to 1100 °C for 1 h, followed by rapid cooling to 100 °C with compressed air for 10 min. At the end of each cycle, digital image records of the sample surfaces were made to assess the number of cycles until failure. The TCF tests were performed on three samples of each kind of TBC system. The coating failure threshold considered was 20% coating spallation, and accordingly, the number of cycles to failure was averaged with the associated standard deviation. The temperature profile for the TCF test is shown in Figure 3.

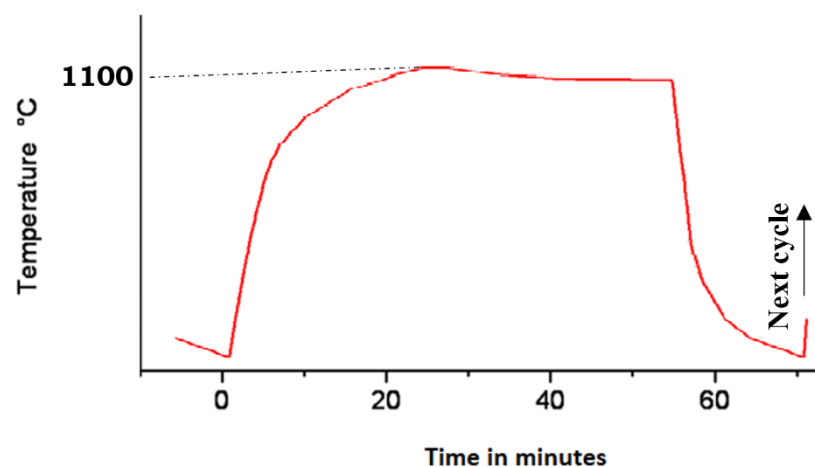


**Figure 3.** Temperature profile for TCF test.

## 3. Results and Discussion

### 3.1. Surface Roughness Measurements

The roughness of the substrate and bond coat can significantly impact the microstructures of the bond coat and topcoat, as well as the adhesion between the substrate and bond coat, and hence the functional performance of TBC. The roughness measurements were performed on H282 forged and AM substrates with and without a bond coat. Figure 4 shows a bar chart representing the roughness values (Ra) obtained by the WLI method. It is

found that the surface roughness of the uncoated forged substrate is very low ( $R_a = 1.5 \mu\text{m}$ ), whereas the roughness measured for the AM substrate is relatively very high ( $R_a = 41.33 \mu\text{m}$ ). A high roughness value is typical for the AM substrates, and it is mainly due to peaks and valleys formed by unmelted powder particles during the AM process. The roughness value ( $R_a = 11.31 \mu\text{m}$ ) measured for the APS bond coat on the reference substrate is typical for the APS process on a forged substrate. More interestingly, the roughness measured on HVAF and APS bond coats on AM substrates was found to be reduced from  $R_a = 41$  to  $13 \mu\text{m}$ . It is obvious that HVAF/APS coated bond coat masks the surface irregularities of the AM built surface and facilitates perfect anchoring sites for the impending YSZ topcoat. Thus, it can be inferred that the bond coat deposited by APS increases the surface roughness of the reference substrate, whereas the bond coat deposited by HVAF and APS decreases the surface roughness of the AM substrates.

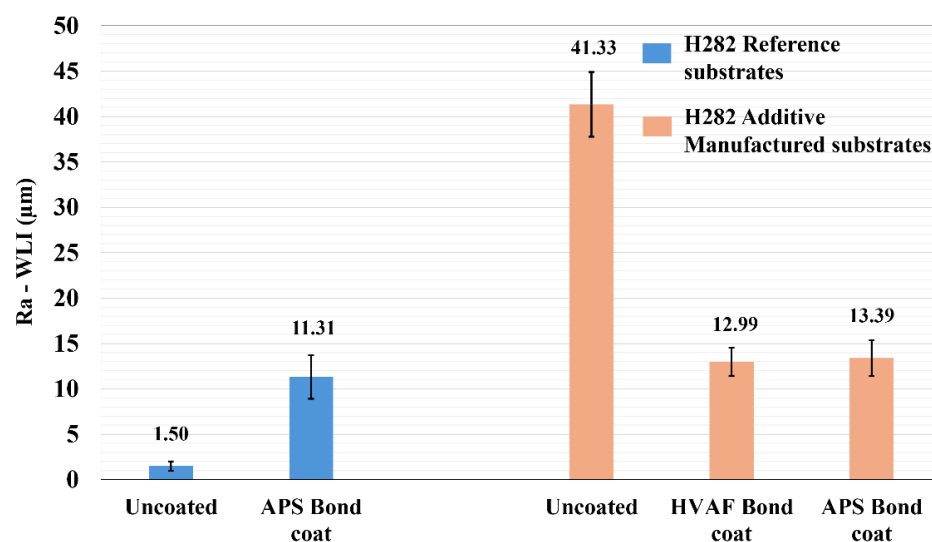


**Figure 4.** Bar chart showing arithmetic average roughness  $R_a$  measured for substrate and bond coat by WLI method.

### 3.2. Porosity Evaluation

The porosity measurement results of the APS YSZ coating developed at four test runs (Table 4-Run 1–4) with different combinations of substrate surface condition (AM vs. reference), bond coat deposition technique (HVAF with fine NiCoCrAlY powder and APS with coarse NiCoCrAlY powder), YSZ powder morphology (A&S and HOSP), YSZ spray process (radial feed and axial feed) are presented in Figure 5. The corresponding YSZ cross-sectional images confirming the porosity features are shown in Figure 6. In Run 1 and 4, the YSZ feedstock (AMP827 A&S) deposited by the F4 gun (radial) and the YSZ feedstock (AMP827 A&S) deposited by the axial III gun, respectively, exhibited the highest porosity (porosity = 16%–20%). The higher feed rate observed for A&S powder with high-volume feed, in turn, may have allowed for the greater porosity transfer to the coating during deposition. From SEM analysis, it can also be inferred that there is a large degree of globular porosity that is typical for an agglomerated and sintered spray powder coating [26]. Whereas in Run 2 and 3, the YSZ feedstock AMP831–plasma spheroidized HOSP powder due to their spherical shape and better flowability, resulting in a modest improvement in the microstructure (porosity = 10%–15%). However, it does not seem that the use of (AM/forged) substrate, bond coat (APS/HVAF) or feedstock injection (axial/radial) has an impact on the porosity of the APS–YSZ topcoat.

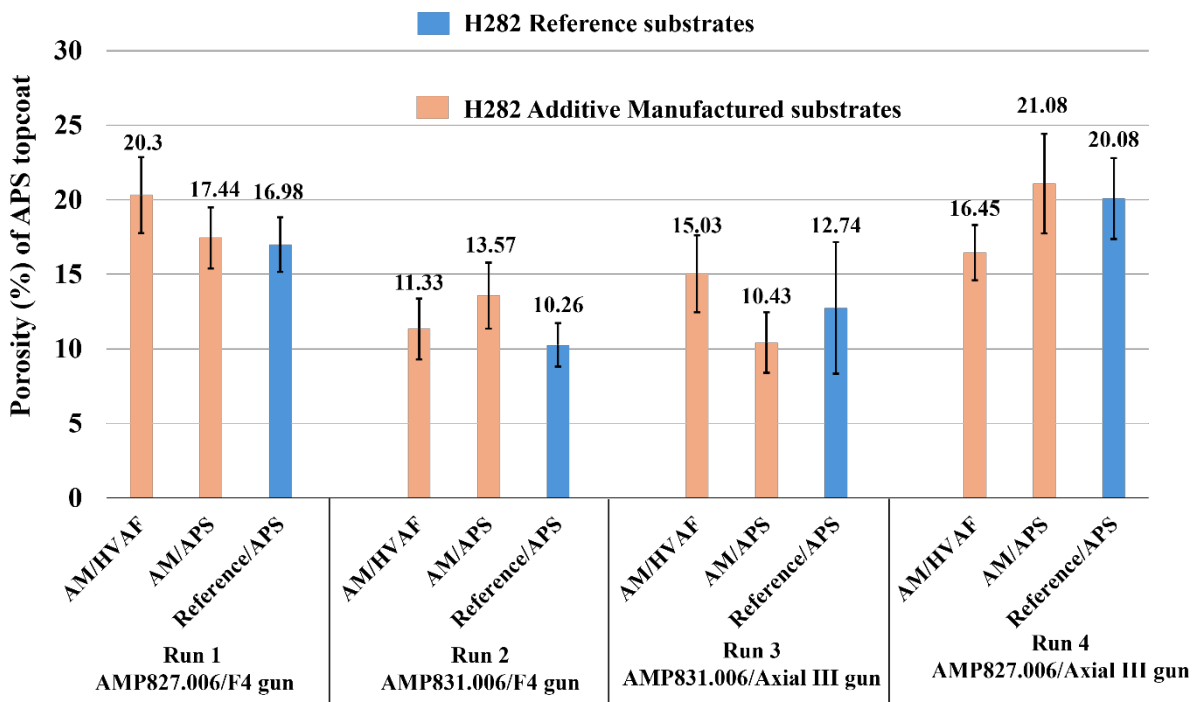


Figure 5. Porosity distribution in APS topcoats measured by image analysis for Run 1 to Run 4.

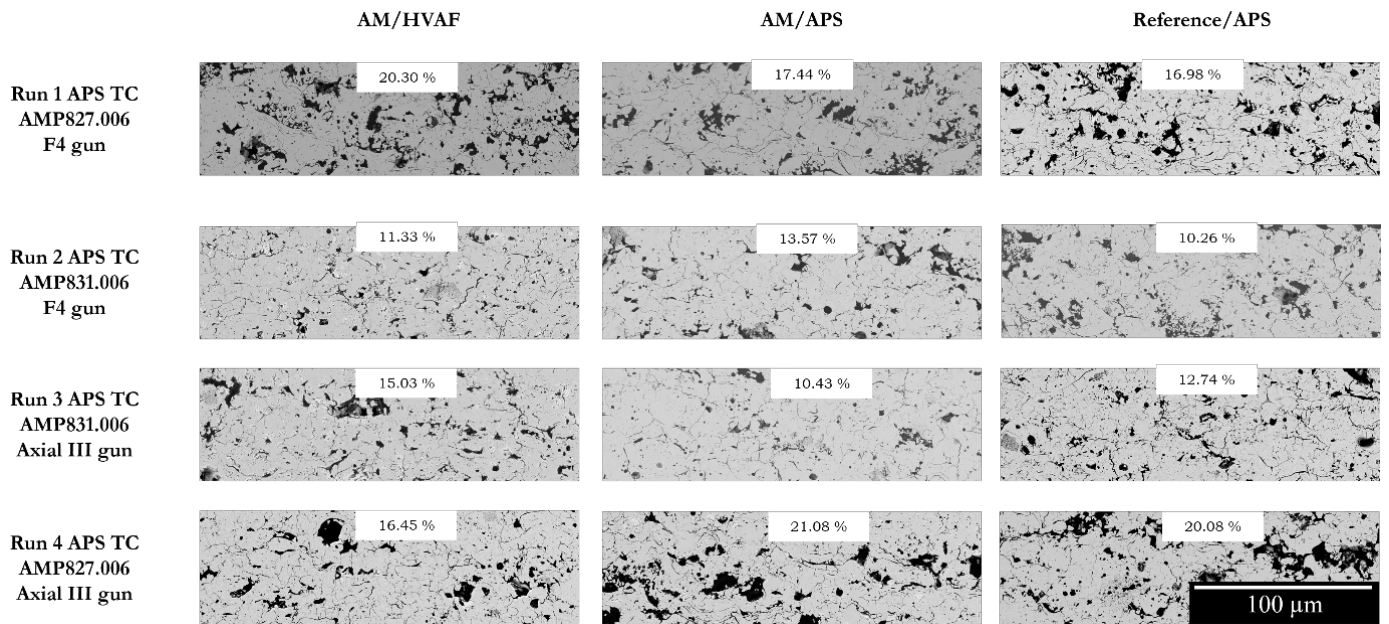


Figure 6. SEM images of the porosity distribution of APS topcoat for Run 1 to 4 with two different YSZ feedstock powder morphology and spray gun.

### 3.3. Microstructural Characterizations

The systematic investigation on the influence of substrate surface condition (AM vs. reference), bond coat deposition technique (HVAF with fine NiCoCrAlY powder and APS with coarse NiCoCrAlY powder), YSZ powder morphology (A&S and HOSP), and YSZ spray process (radial feed and axial feed) on APS topcoat microstructure evolution is presented in the following three sections. The first part discusses the effect of substrate surface condition (AM vs. reference) and bond coat deposition technique (HVAF/APS-NiCoCrAlY) on topcoat (APS-YSZ) microstructure. The second part is dedicated to understanding the impact of using different YSZ feedstock powder morphology (A&S/HOSP) on the

microstructure evolution of YSZ topcoat. The third part discusses the impact of the YSZ spray process (F4 MB radial and Axial III spray gun) on the YSZ topcoat microstructure.

### 3.3.1. Effect of Different Substrates and Bond Coat on Topcoat Microstructure

Figure 7 shows the SEM cross-sectional images of APS–YSZ (AMPERIT831.006 powder) topcoat with HVOF/APS–NiCoCrAlY bond coat on AM and reference substrates. In all the cases, APS–YSZ coating exhibits characteristic lamellar structures with inherent porosities of 10%–13%, proven to be optimum porosity with excellent thermal barrier and high thermal strain tolerance coatings for high-temperature applications [27,28]. As discussed in Section 3.1, the roughness of AM substrates ( $R_a = 41.33 \mu\text{m}$ ) is observed to be much higher than that of reference substrates ( $R_a = 1.5 \mu\text{m}$ ). Thus, the SEM cross-sectional image in Figure 7 also confirmed the presence of AM-built-induced defects at the AM substrate and bond coat interface, labelled as porosities created by the deep and sharp cavities of the rough surface (Figure 7a) and unmelted H282 powder particles (Figure 7b).

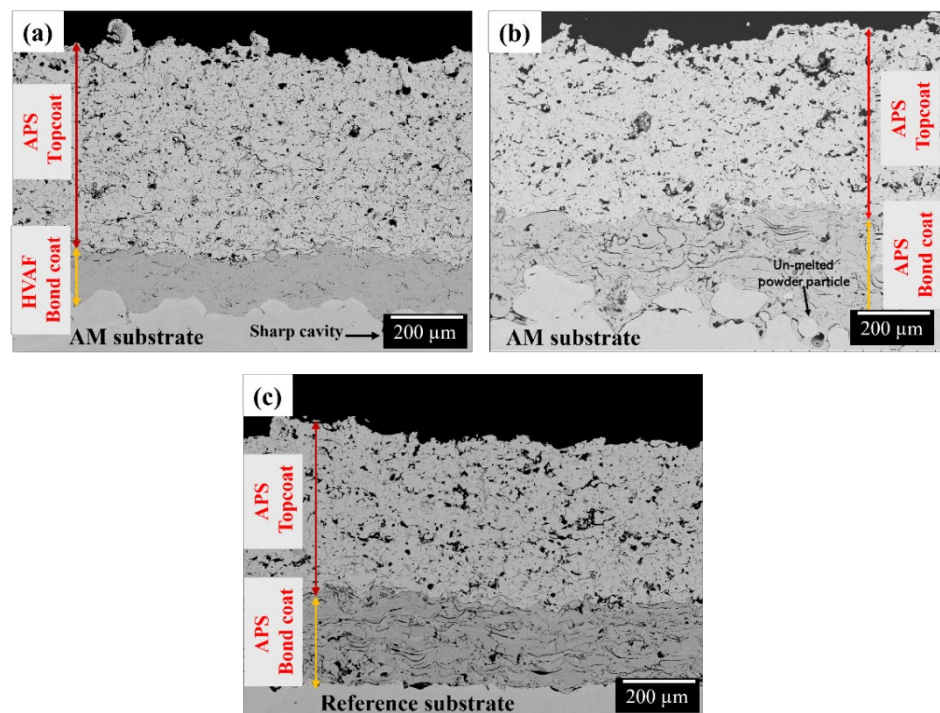


**Figure 7.** SEM cross-sectional micrograph of (a) AM substrate + HVOF bond coat + APS topcoat; (b) AM substrate + APS bond coat + APS topcoat; (c) reference substrate + APS bond coat + APS topcoat.

However, despite the use of two distinct substrates (AM and reference), the disparity in roughness values at the bond coat–topcoat interface appears to be much lower ( $R_a = 11\text{--}13 \mu\text{m}$ ) when comparing TBCs on reference and AM substrates. Also, Figure 7 confirms a denser HVOF bond coat, whereas the APS-deposited bond coat is less dense with interlamellar porosity and oxides. In other words, the HVOF-processed bond coat possesses minimal in situ feedstock oxidation due to a relatively lower operating temperature (compared to APS) [29,30]. Thus, due to the influence of the AM/forged substrate finish and APS/HVOF processed bond coat, no substantial changes in topcoat microstructure were noticed.

### 3.3.2. Impact of Using Different YSZ Feedstock Powder Morphology

Figure 8 shows the SEM cross-sectional micrograph of the APS-YSZ topcoat on AM substrates with HVOF–NiCoCrAlY bond coat. The interaction between the feedstock and the thermal spray heat source is influenced by powder morphology, which in turn affects

the microstructure of the coating and hence its overall endurance and performance. To ensure good comparability between the different feedstocks, YSZ coatings were deposited by APS using an F4-MB gun for each feedstock powder. The porosity measured for the YSZ topcoat was found to be 20% for AMP827.006 (A&S) and 11% for AMP831.006 (HOSP). The difference in porosity level in YSZ coating is solely related to the feedstock powder processing methods. This observation was also supported by Streibl et al. [31], wherein they examined the in-flight temperature and velocity of commercial HOSP, fused and crushed A&S feedstock powders, and correlated them with coating microstructures. It was observed that HOSP particles were indeed the easiest to melt, with higher deposition efficiency and less porosity compared to other powder morphologies. Thus, the YSZ topcoat microstructure does not seem to be influenced by the substrate surface (AM/reference), bond coat deposition method (APS/HVAF), or feedstock injection (axial/radial).

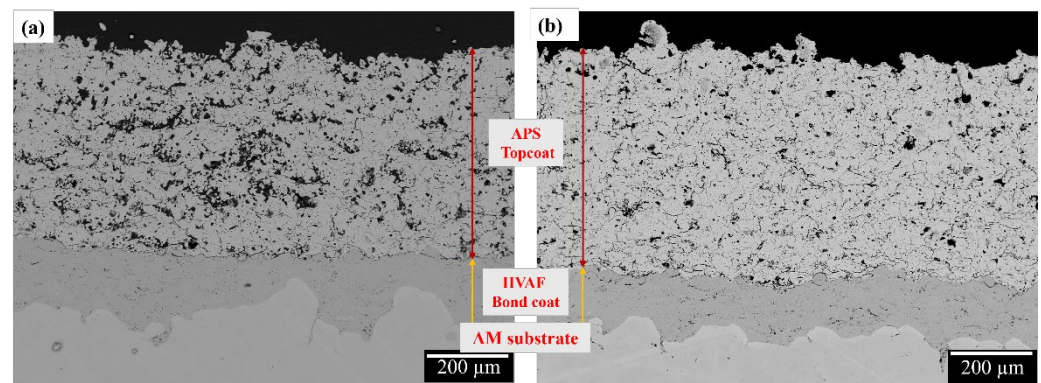


**Figure 8.** SEM micrograph of AM substrate + HVAF bond coat + APS topcoat. (a) Run 1: AMP827.006/F4-MB; (b) Run 2: AMP831.006/F4-MB.

### 3.3.3. Impact of Using Different Spray Guns

SEM cross-sectional micrographs of APS-YSZ top coating deposited by radial and axial spray guns on AM substrates with HVAF-NiCoCrAlY bond coat are shown in Figure 9a,b, respectively. The YSZ coating developed by radial injection was found to exhibit a relatively higher porous coating (porosity = 20%) than axial injection (porosity = 16%). This may be due to the long residence time (rapid heat up) offered by the axial injection as compared to the radial injection spray gun. The higher the residence time of the feedstock in the high-temperature part of the jet, the higher the degree of feedstock-flame interaction, the higher the particle velocity and the denser the coating [32]. This also confirms the YSZ microstructure characteristic features majorly depend on the spray process employed (radial or axial feed) rather than the type of substrate used.

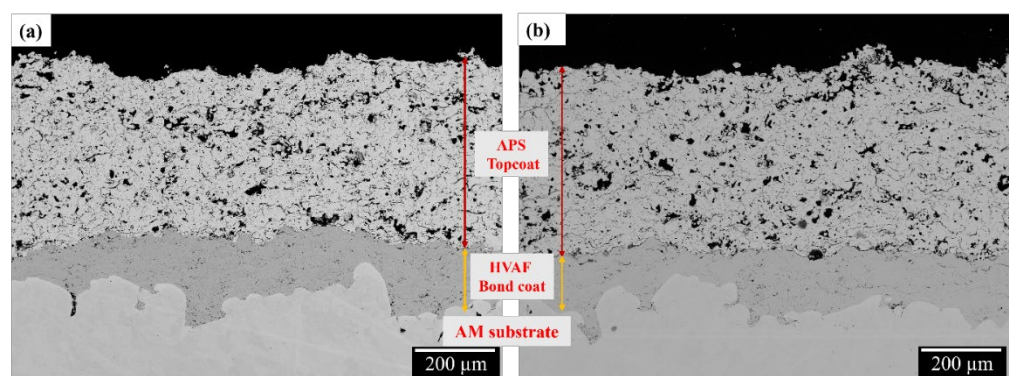


**Figure 9.** SEM cross-sectional micrograph of AM substrate + HVAF bond coat + APS topcoat. (a) Run 1: AMP827.006/F4 MB spray gun-radial feed; (b) Run 4: AMP827.006/Axial III spray gun-axial feed.

### 3.4. Erosion Testing

The YSZ topcoats of each of the eight TBC systems (on AM substrates) were subjected to erosion testing, and the erosion rate bar chart is shown in Figure 10. In general, the topcoat erosion rate is determined by its porosity, roughness, and coating cohesion strength. It is obvious that the higher the porosity, the easier it is for the erosive media to erode the coating and thus, the higher the erosion rate [14,18]. From the erosion study, it is confirmed that the highly porous Run 4 AM/HVAF and AM/APS (A&S feedstock) showed higher erosion rates. At the same time, the less porous Run 3 AM/HVAF and AM/APS (HOSP) exhibited lower erosion rates. It can be inferred that the use of (AM/reference) substrates and bond coats (APS/HVAF), does not show a significant impact on the erosion rate of the APS–YSZ topcoat.

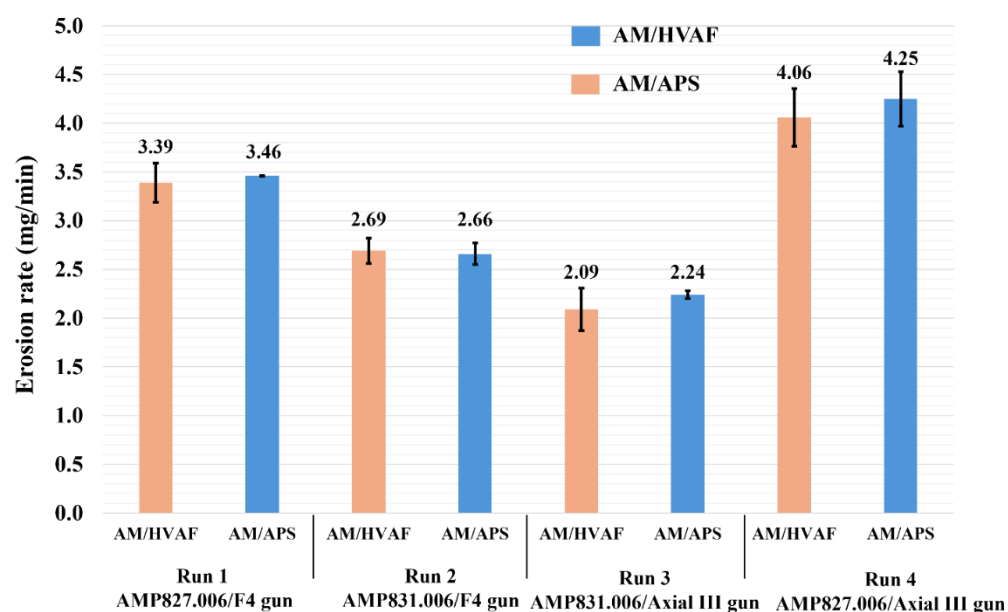
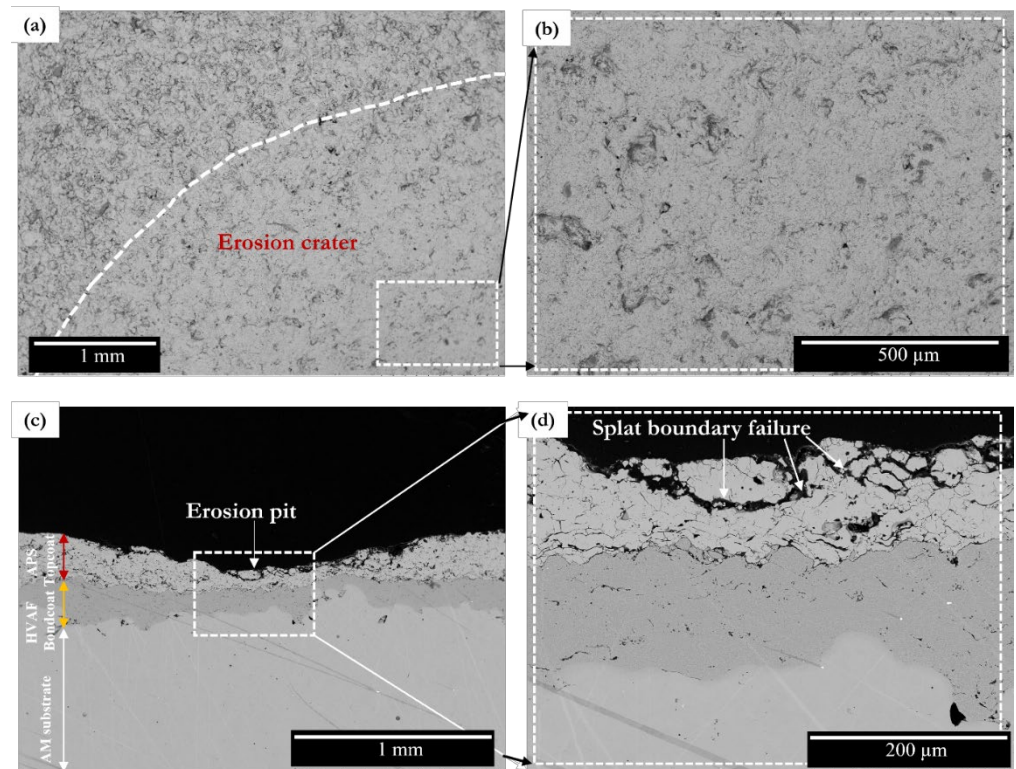


Figure 10. Bar chart representing erosion rate (mg/min) of the TBC on AM substrates.

Post-erosion microstructure analysis of the highest-eroded sample (Run 4 AM/HVAF) is further investigated by SEM surface and cross-sectional analysis. Figure 10 displays the SEM surface (Figure 11a,b) and cross-sectional micrographs (Figure 11c,d) of a 90-degree erosion impact pit for Run 4 AM/HVAF with APS topcoat. Figure 11a shows an eroded surface with a smoother surface as compared to the non-eroded region, as it confirms that the erodent removes the material from the rough surface and structurally weaker splats. The magnified view reveals erosion scars with even patterns of erodent impact damage, as shown in Figure 11b.

Low-magnification cross-sectional SEM micrograph of a 90-degree erosion impact pit for Run 4 AM/HVAF with APS topcoat confirmed that the erosion of coating was restricted to the YSZ topcoat, and erosion results were reliable even for the highest-eroded sample, as shown in Figure 11c. The high magnification SEM micrographs of the coating cross-section shown in Figure 11d depict material removal due to splat fracture, splat boundary failure, and delamination of the coating during the erodent normal impact. Similar erosion mechanisms were discussed elsewhere [33,34] and complemented the APS YSZ erosion observation. Figure 11d also confirms that upon normal impact, the kinetic energy of the erodent transmitted to the APS YSZ surface causes splat fracture.



**Figure 11.** SEM micrographs, the 90-degree erosion impact pit for Run 4 AM/HVOF with APS topcoat: (a) low-magnification eroded surface revealing erosion crater with a smooth surface finish as compared to pristine surface; (b) magnified view of erosion crater as highlighted in (a); (c) cross-sectional micrograph revealing erosion pit formation at the YSZ topcoat; (d) magnified view of erosion pit as highlighted in (c) confirming erosion mechanism.

### 3.5. Thermal Cyclic Fatigue Analysis

Microstructure characterization and erosion tests clearly revealed that powder feedstock morphology and spray gun play a major role in YSZ microstructure, and functional properties rather than the substrate employed. Thus, the TCF test has been attempted for the YSZ coating with varying bond coat deposition methods, spray gun and powder feedstock morphology. Figure 12 shows the results of TCF lifetime for the YSZ topcoat sprayed at two different powder feedstock morphology and spray guns with NiCoCrAlY bond coat deposited by HVOF and APS. Runs 1 and 4 with YSZ coatings deposited by A&S feedstock powder were found to show the highest lifetime, whereas Runs 2 and 3 with YSZ coatings deposited by HOSP feedstock powder exhibited the lowest lifetime on both AM and standard substrate. On prolonged exposure at elevated temperatures, the driving force for the coating failure is the combination of the thermal mismatch stresses between the coating and the substrate, sintering of the topcoat, and growth of thermally grown oxide (TGO) at the bond coat–topcoat interface [4,14]. As the HVOF bond coat oxidation behaviour is the same for all TCF-tested samples, it can be deduced that topcoat microstructures may also result in varying TCF lifetime. It could be expected that the increased TCF lifetime for Run 1 and Run 4 on both the AM and reference substrates may be due to higher porosity levels with greater stress relaxation during cycling [35,36].

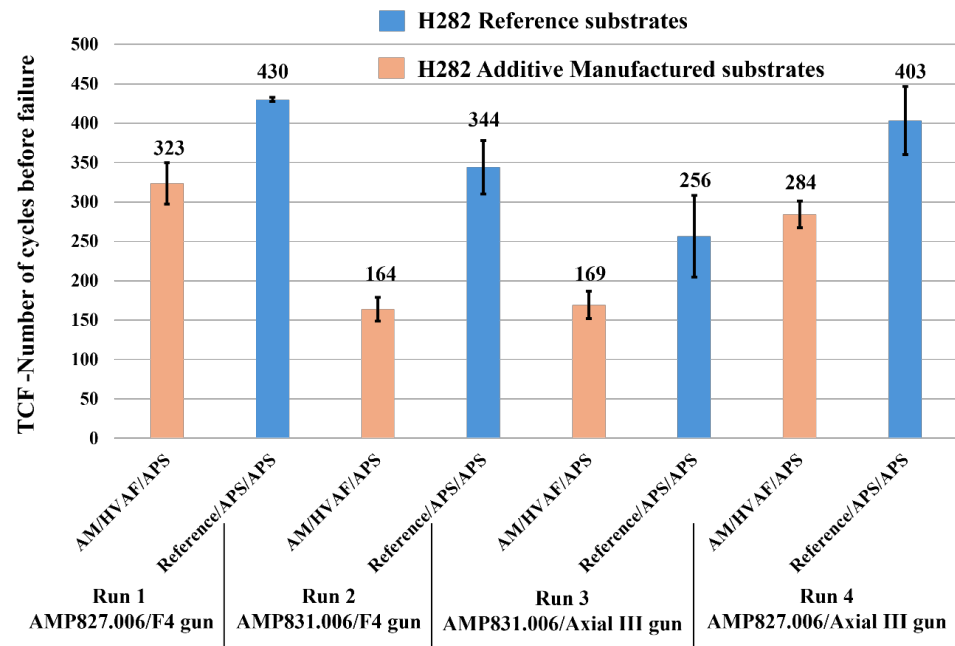


**Figure 12.** Bar chart representing thermal cyclic fatigue lifetime/number of cycles before failure of the TBC on AM and reference substrates.

Further, the TGO analysis of coating was carried out for the TCF-tested sample (Run 4 AM/HVAF/APS), as shown in Figure 13. SEM backscattered image and elemental mapping confirmed the formation of TGO comprised of alumina ( $Al_2O_3$ ) at the topcoat–bond coat interface, also supported by EDS analysis (Figure 13c,f). After the TCF test, since the YSZ coating had completely spalled off from the substrate for all the samples, the TGO formation was examined in spalled-off coating at the topcoat–TGO interface and bond coat–TGO interface. The growth of TGO introduces thermal expansion mismatch and, ultimately, stress generation at the topcoat–TGO interface. This, in turn, causes the generation of fatigue cracks, which further facilitates heat and oxygen to reach the bond coat, contributing to the thickening of TGO [14].

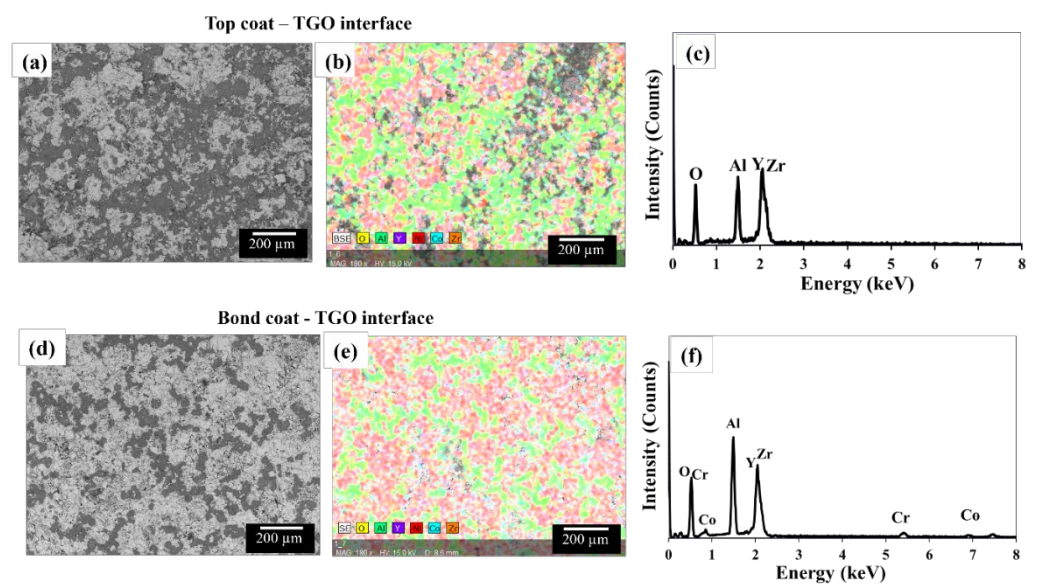


**Figure 13.** SEM surface morphology, EDS elemental mapping, and elemental confirmation of TCF tested (Run 4 AM/HVAF/APS) coating: (a–c) topcoat–TGO interface; (d–f) bond coat–TGO interface.

Thus, it confirms that the lack of TGO adhesion to either topcoat or bond coat may cause the complete spallation of the YSZ topcoat. However, the thickness of the TGO layer seems inhomogeneous; specifically, in the spalled-off coating, TGO greatly adheres to the YSZ topcoat (Figure 13a,b) compared to the bond coat (Figure 13d,e). Despite different topcoat porosity levels, a similar trend in TGO composition distribution was observed in all the TCF-tested samples.

#### 4. Conclusions

The characteristics and performance of APS-deposited YSZ coatings on reference and AM-derived H282 substrates, with NiCoCrAlY bond coats deposited by HVAF and APS routes, have been systematically investigated. The influence of substrate surface condition (AM vs. reference), bond coat deposition technique (HVAF with fine MCrAlY powder and APS with coarse MCrAlY powder), YSZ powder morphology (agglomerated and sintered and HOSP), YSZ spray process (radial feed and axial feed) on YSZ microstructure, and thermal stability performance has been explored. The following are the primary findings of this study:

- Additively manufactured substrates exhibit higher roughness ( $\sim Ra = 41 \mu\text{m}$ ) compared to reference substrates ( $\sim Ra = 1.5 \mu\text{m}$ ), but bond coat deposition reduces roughness to produce suitable surfaces ( $\sim 11\text{--}13 \mu\text{m}$ ) for top YSZ coating deposition.
- Regardless of substrate surface finish, the interface roughness between the bond coat and topcoat remains consistent ( $\sim Ra = 11\text{--}13 \mu\text{m}$ ) across different bond coat deposition methods (HVAF or APS).
- The use of different YSZ powder morphologies results in varying porosity levels in the topcoats, with HOSP YSZ coatings exhibiting lower porosity (10%–15%) compared to agglomerated and sintered YSZ coatings (16%–21%).
- Changing the spray gun from radial to axial injection does not significantly affect YSZ coating performance in erosion rate and TCF lifetime, but axial spray gun deposition results in denser microstructure (porosity = 16%) compared to radial injection (porosity = 20%) for YSZ coating.
- The YSZ microstructure (porosity level) significantly influences erosion and TCF lifetime performance, while the effects of bond coat deposition techniques, spray gun, or substrate type (reference/AM) are minimal.

Thus, it can be inferred that the characteristic microstructural and functional properties of ceramic topcoat on AM substrates may be matched to those of reference (forged) substrates by achieving adequate porosity on AM substrates by using suitable spray gun and feedstock powder morphology.

**Author Contributions:** Conceptualization, M.B., X.-H.L. and R.F.; Methodology, M.B. and S.B.; Validation, S.J. and N.M.; Formal analysis, M.B.; Investigation, M.B.; Resources, X.-H.L., R.F. and B.K.; Data curation, M.B. and S.B.; Writing—original draft, M.B.; Writing—review & editing, M.B., S.B., X.-H.L., R.F., B.K., S.J. and N.M.; Supervision, S.J. and N.M.; Project administration, X.-H.L., S.J. and N.M.; Funding acquisition, X.-H.L., R.F., B.K., S.J. and N.M. All authors have read and agreed to the published version of the manuscript.

**Funding:** Financial support from the Knowledge Foundation, Sweden, for the project Engineered coatings for next generation gas turbine components (EcoGATE) (Dnr. 2020007), as a part of which the present work was carried out, is gratefully acknowledged.

**Data Availability Statement:** Data are contained within the article.

**Acknowledgments:** The authors would like to thank their colleagues at University West, Manon Florent for experimental assistance, Jonas Olsson for producing the AM substrates and Magnus Sandberg for assistance during spraying of coatings.

**Conflicts of Interest:** The authors declare that they have no known competing financial interests or personal relationships that could have appeared to influence the work reported in this paper.

## References

1. Yin, F.; Rao, A.G. A Review of Gas Turbine Engine with Inter-Stage Turbine Burner. *Prog. Aerosp. Sci.* **2020**, *121*, 100695. [CrossRef]
2. Tejero-Martin, D.; Bennett, C.; Hussain, T. A Review on Environmental Barrier Coatings: History, Current State of the Art and Future Developments. *J. Eur. Ceram. Soc.* **2021**, *41*, 1747–1768. [CrossRef]
3. Stefan, E.; Talic, B.; Larring, Y.; Gruber, A.; Peters, T.A. Materials Challenges in Hydrogen-Fuelled Gas Turbines. *Int. Mater. Rev.* **2022**, *67*, 461–486. [CrossRef]
4. Osorio, J.D.; Toro, A.; Hernández-Ortiz, J.P. Thermal Barrier Coatings for Gas Turbine Applications: Failure Mechanisms and Key Microstructural Features. *DYNA* **2012**, *79*, 149–158.
5. Otto, R.; Brøtan, V.; Carvalho, P.A.; Reiersen, M.; Graff, J.S.; Sunding, M.F.; Berg, O.Å.; Diplas, S.; Azar, A.S. Roadmap for Additive Manufacturing of HAYNES®282® Superalloy by Laser Beam Powder Bed Fusion (PBF-LB) Technology. *Mater. Des.* **2021**, *204*, 109656. [CrossRef]
6. Gebisa, A.W.; Lemu, H.G. Additive manufacturing for the manufacture of gas turbine engine components: Literature review and future perspectives. In Proceedings of the ASME Turbo Expo 2018: Turbomachinery Technical Conference and Exposition, Oslo, Norway, 11–15 June 2018.
7. Pike, L.M. Development of a fabricable gamma-prime ( $\gamma'$ ) strengthened superalloy. *Superalloys* **2008**, *2008*, 191–200.
8. Sanchez, S.; Smith, P.; Xu, Z.; Gaspard, G.; Hyde, C.J.; Wits, W.W.; Ashcroft, I.A.; Chen, H.; Clare, A.T. Powder Bed Fusion of Nickel-Based Superalloys: A Review. *Int. J. Mach. Tools Manuf.* **2021**, *165*, 103729. [CrossRef]
9. Grzegorz Gawel, T. Review of Additive Manufacturing Methods. *Solid State Phenom.* **2020**, *308*, 1–20.
10. Sadeghi, E.; Karimi, P.; Momeni, S.; Seifi, M.; Eklund, A.; Andersson, J. Influence of Thermal Post Treatments on Microstructure and Oxidation Behavior of EB-PBF Manufactured Alloy 718. *Mater. Charact.* **2019**, *150*, 236–251. [CrossRef]
11. Alehojat, M.; Jafari, R.; Karimi, P.; Sadeghi, E. Electron Beam-Powder Bed Fusion of Alloy 718: Effect of Hot Isostatic Pressing and Thermal Spraying on Microstructural Characteristics and Oxidation Performance. *Surf. Coat. Technol.* **2020**, *404*, 126626. [CrossRef]
12. Varis, T.; Mäkelä, A.; Suhonen, T.; Laurila, J.; Vuoristo, P. Integrity of APS, HVOF and HVOF Sprayed NiCr and NiCrBSi Coatings Based on the Tensile Stress-Strain Response. *Surf. Coat. Technol.* **2023**, *452*, 129068. [CrossRef]
13. Feuerstein, A.; Knapp, J.; Taylor, T.; Ashary, A.; Bolcavage, A.; Hitchman, N. Technical and Economical Aspects of Current Thermal Barrier Coating Systems for Gas Turbine Engines by Thermal Spray and EBPVD: A Review. *J. Therm. Spray Technol.* **2008**, *17*, 199–213. [CrossRef]
14. Bellippady, M.; Florent, M.; Björklund, S.; Li, X.H.; Robert, F.; Kjellman, B.; Joshi, S.; Markocsan, N. Characteristics and Performance of Suspension Plasma Sprayed Thermal Barrier Coatings on Additively Manufactured Superalloy Substrates. *Surf. Coat. Technol.* **2023**, *472*, 129926. [CrossRef]
15. Markocsan, N.; Nylén, P.; Wigren, J.; Li, X.H. Low Thermal Conductivity Coatings for Gas Turbine Applications. *J. Therm. Spray Technol.* **2007**, *16*, 498–505. [CrossRef]
16. Curry, N.; VanEvery, K.; Snyder, T.; Markocsan, N. Thermal Conductivity Analysis and Lifetime Testing of Suspension Plasma-Sprayed Thermal Barrier Coatings. *Coatings* **2014**, *4*, 630–650. [CrossRef]
17. Ang, A.S.M.; Berndt, C.C. A Review of Testing Methods for Thermal Spray Coatings. *Int. Mater. Rev.* **2014**, *59*, 179–223. [CrossRef]
18. Shi, M.; Xue, Z.; Zhang, Z.; Ji, X.; Byon, E.; Zhang, S. Effect of Spraying Powder Characteristics on Mechanical and Thermal Shock Properties of Plasma-Sprayed YSZ Thermal Barrier Coating. *Surf. Coat. Technol.* **2020**, *395*, 125913. [CrossRef]
19. Kavaliauskas, Ž.; Keželis, R.; Milieška, M.; Marcinauskas, L.; Valinčius, V.; Aikas, M.; Uscila, R.; Baltušnikas, A.; Žunda, A. Influence of Different Plasma Spraying Methods on the Physical Properties of YSZ Coatings. *Surf. Interfaces* **2021**, *24*, 101120. [CrossRef]
20. Curry, N. *Design of Thermal Barrier Coating Systems*; University West: Hong Kong, China, 2014; ISBN 9789197794398.
21. Powders for Thermal Spraying AMPERIT®405. Available online: <https://www.hoganas.com/en/powder-technologies/additive-manufacturing-metal-powders/amperprint/> (accessed on 11 February 2024).
22. Dadfar, M.R.; Rahimpour, M.R.; Vaezi, M.R.; Gholamzadeh, A. Characterization and Phase Transformation of Spherical YSZ Powders Fabricated Via Air Plasma Spray Method. *Adv. Ceram. Prog.* **2016**, *2*, 32–38.
23. Polkowska, A.; Polkowski, W.; Warmuzek, M.; Cieśla, N.; Włoch, G.; Zasada, D.; Purgert, R.M. Microstructure and Hardness Evolution in Haynes 282 Nickel-Based Superalloy During Multi-Variant Aging Heat Treatment. *J. Mater. Eng. Perform.* **2019**, *28*, 3844–3851. [CrossRef]
24. ISO 21920-2:2021 Geometrical Product Specifications (GPS)-Surface Texture: Profile. Available online: <https://www.iso.org/standard/72226.html> (accessed on 9 May 2024).
25. ASTM International. *G76, Standard Test Method for Conducting Erosion Tests by Solid Particle Impingement Using Gas Jets*; ASTM International: West Conshohocken, PA, USA, 2013.
26. Curry, N.; Leitner, M.; Körner, K. High-Porosity Thermal Barrier Coatings from High-Power Plasma Spray Equipment—Processing, Performance and Economics. *Coatings* **2020**, *10*, 957. [CrossRef]
27. Salman, A.; Ghadiri, M.; Hounslow, M. *Handbook of Powder Technology: Particle Breakage*; Elsevier: Amsterdam, The Netherlands, 2007.
28. Davis, J.R. *Handbook of Thermal Spray Technology*; ASM International: Materials Park, OH, USA, 2004; ISBN 0871707950.

29. Matikainen, V.; Koivuluoto, H.; Vuoristo, P. A Study of Cr<sub>3</sub>C<sub>2</sub>-Based HVOF- and HVAF-Sprayed Coatings: Abrasion, Dry Particle Erosion and Cavitation Erosion Resistance. *Wear* **2020**, *446*, 203188. [[CrossRef](#)]
30. Mahade, S.; Aranke, O.; Björklund, S.; Dizdar, S.; Awe, S.; Mušálek, R.; Lukáč, F.; Joshi, S. Influence of Processing Conditions on the Microstructure and Sliding Wear of a Promising Fe-Based Coating Deposited by HVAF. *Surf. Coat. Technol.* **2021**, *409*, 126953. [[CrossRef](#)]
31. Streibl, T.; Vaidya, A.; Friis, M.; Srinivasan, V.; Sampath, S. A Critical Assessment of Particle Temperature Distributions during Plasma Spraying: Experimental Results for YSZ. *Plasma Chem. Plasma Process.* **2006**, *26*, 73–102. [[CrossRef](#)]
32. Zhou, D.; Guillon, O.; Vaßen, R. Development of YSZ Thermal Barrier Coatings Using Axial Suspension Plasma Spraying. *Coatings* **2017**, *7*, 120. [[CrossRef](#)]
33. Mahade, S.; Venkat, A.; Curry, N.; Leitner, M.; Joshi, S. Erosion Performance of Atmospheric Plasma Sprayed Thermal Barrier Coatings with Diverse Porosity Levels. *Coatings* **2021**, *11*, 86. [[CrossRef](#)]
34. Eaton, H.E.; Novak, R.C. Particulate erosion of plasma-sprayed porous ceramic. *Surf. Coat. Technol.* **1987**, *30*, 41–50. [[CrossRef](#)]
35. Giolli, C.; Scrivani, A.; Rizzi, G.; Borgioli, F.; Bolelli, G.; Lusvarghi, L. Failure Mechanism for Thermal Fatigue of Thermal Barrier Coating Systems. *J. Therm. Spray Technol.* **2009**, *18*, 223–230. [[CrossRef](#)]
36. Scrivani, A.; Rizzi, G.; Bardi, U.; Giolli, C.; Miranda, M.M.; Ciattini, S.; Fossati, A.; Borgioli, F. Thermal Fatigue Behavior of Thick and Porous Thermal Barrier Coatings Systems. *J. Therm. Spray Technol.* **2007**, *16*, 816–821. [[CrossRef](#)]

**Disclaimer/Publisher's Note:** The statements, opinions and data contained in all publications are solely those of the individual author(s) and contributor(s) and not of MDPI and/or the editor(s). MDPI and/or the editor(s) disclaim responsibility for any injury to people or property resulting from any ideas, methods, instructions or products referred to in the content.